

Article

# Modeling and Simulation of a TFET-Based Label-Free Biosensor with Enhanced Sensitivity

Sagarika Choudhury <sup>1,\*</sup>, Krishna Lal Baishnab <sup>1</sup>, Koushik Guha <sup>1</sup>, Zoran Jakšić <sup>2</sup>, Olga Jakšić <sup>2</sup>  
and Jacopo Iannacci <sup>3,\*</sup>

<sup>1</sup> Department of Electronics and Communication Engineering, National Institute of Technology, Silchar 788010, India; koushik@ece.nits.ac.in

<sup>2</sup> Center of Microelectronic Technologies, Institute of Chemistry, Technology and Metallurgy, National Institute of the Republic of Serbia, University of Belgrade, 11000 Belgrade, Serbia

<sup>3</sup> Center for Sensors and Devices (SD), Fondazione Bruno Kessler (FBK), 38123 Trento, Italy

\* Correspondence: sagarika\_rs@ece.nits.ac.in (S.C.); iannacci@fbk.eu (J.I.)

**Abstract:** This study discusses the use of a triple material gate (TMG) junctionless tunnel field-effect transistor (JLTFET) as a biosensor to identify different protein molecules. Among the plethora of existing types of biosensors, FET/TFET-based devices are fully compatible with conventional integrated circuits. JLTFETs are preferred over TFETs and JLFETs because of their ease of fabrication and superior biosensing performance. Biomolecules are trapped by cavities etched across the gates. An analytical mathematical model of a TMG asymmetrical hetero-dielectric JLTFET biosensor is derived here for the first time. The TCAD simulator is used to examine the performance of a dielectrically modulated label-free biosensor. The voltage and current sensitivity of the device and the effects of the cavity size, bioanalyte electric charge, fill factor, and location on the performance of the biosensor are also investigated. The relative current sensitivity of the biosensor is found to be about  $10^{13}$ . Besides showing an enhanced sensitivity compared with other FET- and TFET-based biosensors, the device proves itself convenient for low-power applications, thus opening up numerous directions for future research and applications.

**Keywords:** biosensors; protein sensing; tunnel field-effect transistor; TFET; junctionless TFET; triple material gate; TCAD simulation

**Citation:** Choudhury, S.; Baishnab, K.L.; Guha, K.; Jakšić, Z.; Jakšić, O.; Iannacci, J. Modeling and Simulation of a TFET-Based Label-Free Biosensor with Enhanced Sensitivity. *Chemosensors* **2023**, *11*, 312. <https://doi.org/10.3390/chemosensors11050312>

Academic Editor: Camelia Bala

Received: 18 March 2023

Revised: 18 May 2023

Accepted: 21 May 2023

Published: 22 May 2023



**Copyright:** © 2023 by the authors. Licensee MDPI, Basel, Switzerland. This article is an open access article distributed under the terms and conditions of the Creative Commons Attribution (CC BY) license (<https://creativecommons.org/licenses/by/4.0/>).

## 1. Introduction

The need for effective biosensors has increased greatly in recent times owing to the COVID-19 pandemic. Although a vast number of different biosensors have been designed to sense analytes such as proteins, toxins, DNA, viruses, bacteria, other pathogens, etc. [1–3], most of these are based on complex techniques that increase the cost as well as the detection time [4,5]. The innumerable existing types of biosensors can be classified based on their transduction mechanisms. Among the sensors widely used today are electrochemical ones [6,7] (genic, etc.), electronic biosensors (typically including variants of FET transistors, e.g., ordinary FET, MOSFET, ISFET, TFET, etc.), and gravimetric ones (thermal, acoustic, etc.) [8–12]. All of the quoted sensor classes have their own sets of advantages and disadvantages, but the most convenient biosensor is hard to find and would depend on a specific application.

Among the quoted devices, electronic biosensors have the advantage of mature fabrication technologies (the family of planar technologies) and their compatibility and integrability with standard silicon-integrated circuits. Our further attention here is dedicated to this class of biosensors.

Many of the existing biosensors suffer from false positives. While designing such devices, one must consider factors such as accuracy, speed, and cost. In solving these issues

for electronic biosensors, dielectric modulation (DM)-based sensors [13] have gained importance, with either label-free [14] or labeled detection techniques. The former makes use of physical parameters such as relative dielectric permittivity to detect the presence of biomolecules, while the latter usually involves a chemical-binding reaction with a receptor. Label-free techniques are preferred as they involve direct detection and are fast, and the sensors based on them are typically reusable. TFET-based biosensors [15–19] that operate on the principle of tunneling with a subthreshold swing (SS) below 60 mV/dec are preferred. In addition, the FET-based biosensors proposed in references [3–5] are much more advantageous owing to their high sensitivity and cost-effectiveness.

A biosensor based on dielectric modulation was designed using a double gate (DG) FET by Narang et al. [20]. This work achieved a relative current sensitivity (defined as the ratio of ON and OFF currents) of  $10^{10}$  for dielectric permittivity values 1–12. A relative current sensitivity of  $10^7$  was reported by Shafi et al. in a virtually doped TFET biosensor [21]. Further, a dopingless TFET biosensor with a current ratio of  $10^{10}$  was described by Anand et al. [22]. A mathematical model for the TFET-based biosensor was presented by Rakhi et al. [23]. An analytical model for a split gate TFET biosensor was proposed by Singh et al. [24].

Because of their inherent operating principle, FET-based biosensors [13,15] suffer from high subthreshold swing (SS) and short-channel effects (SCE). However, in a TFET, it is quite difficult to realize abrupt junctions [25], which are essential for tunneling. Thus, JLTFETs come into the picture. These are basically an amalgamation of two concepts: a JLFET and the tunneling phenomenon. The JLTFET operation is based on the theory of work function modulation [25], where a uniformly doped n-type device with no initial potential barrier is made to behave as a PIN structure. Thus, the process of physical doping is avoided in JLTFETs, and the junctions are created by metal electrodes. Further, a JLTFET incorporates two gates: a polar gate at zero bias for inducing the  $P^+$  region with a high work function metal and a control gate for inducing the channel region by varying the work function. During the OFF state, because of the work function difference, the channel is depleted, and a barrier is created; hence, tunneling is negligible. As suitable gate bias is applied, the electron concentration below the control gate increases, the region becomes n-type, the barrier narrows, the channel is aligned, and tunneling takes place. Thus, the fabrication complexity of a conventional TFET and random dopant fluctuations are avoided in a JLTFET. Hence, JLTFET-based biosensors that have the advantages of TFETs and uniform doping are found to provide much better results than the other types of FET-based sensors. JLTFETs are much easier to fabricate, less prone to short-channel effects (SCE), and have an SS below 60. Chakraborty et al. [26] proposed the a for a surrounding gate JLTFET biosensor operated using the dielectric modulation technique. Gao [27] proposed an ultrasensitive biosensor for point-of-care diagnostics.

Most of the biosensors proposed in the literature suffer from low sensitivity, and realizing abrupt junctions with TFETs is difficult. This work presents a technique to improve the sensitivity of the existing biosensors by using a triple material gate (TMG) asymmetrical hetero-dielectric (AHD) junctionless tunnel field-effect transistor (JLTFET); i.e., it describes a TMG-AHD-JLTFET-based biosensor. Moreover, this work also derives an analytical mathematical model and validates the simulated results. The goal of this research is to determine the highest sensitivity of the proposed device when examining neutral and charged biological molecules. In addition, the impacts of various values of a biomolecule's relative permittivity on the drain current, subthreshold slope, current ratio, and their sensitivity for both neutral and charged biological molecules are investigated.

The paper is organized as follows. First, the design of the device used as a biosensor is described, and then, the workings and development of the mathematical model and simulation procedure are discussed. The paper continues with the analysis of the obtained results. General conclusions are drawn at the end.

## 2. Materials and Methods

The biosensor in this work is designed as a junctionless device with an asymmetrical hetero-dielectric and triple material [28–31] control gate. The biosensor cross-section is shown in Figure 1. The dielectric layer consists of two strata of different materials. High- $k$  and low- $k$  dielectric materials are combined in the top gate dielectric's initial layer, which is followed by a high- $k$  layer. Here,  $k$  denotes relative dielectric permittivity. The lower gate, however, only has a high- $k$  layer of 2 nm thick. In addition, a 2 nm spacer is added between the gates for improved isolation. In addition, a triple material gate (TMG) [28–31], where M1 is aluminum, M2 is cobalt, and M3 is scandium, has the benefit of enhanced gate control and greater carrier mobility, combined with asymmetry in the dielectric for improved performance. The use of high-permittivity material close to the tunneling junction enhances the electric field across the junction, which, in turn, improves the tunneling efficiency and increases the ON current. Similarly to this, using low- $k$  material close to the drain causes the OFF current to drop. Consequently, it has been found that using TMGs with asymmetric hetero-dielectrics considerably improves the current ratio with moderate SS levels. The suggested device is calibrated with a traditional JLTFET [25], as depicted in Figure 2.

The basic operation of the proposed biosensor can be explained by the phenomenon of dielectric modulation [31–35], wherein the change in dielectric material across the cavity enhances the effective coupling across the tunnel junction. This, in turn, changes the overall surface potential and thereby affects the electric field across the tunneling area, which results in an increased output current. The dielectric of the control gate is etched to form a cavity that serves as the entrapment surface of the biosensor. A basic 2 nm layer dielectric is kept intact for isolation purposes, and then, the cavity is etched. The process of etching is similar to the one described in [36].

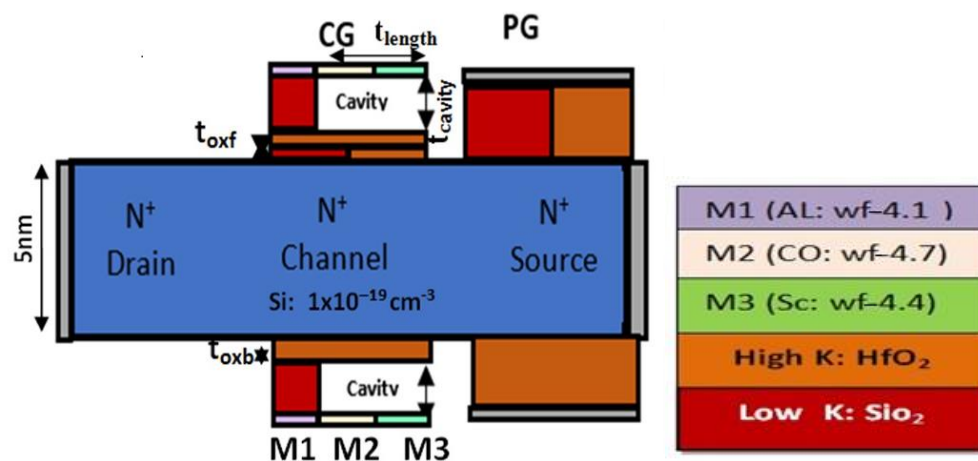


Figure 1. Proposed DM-JLTFET as a biosensor.

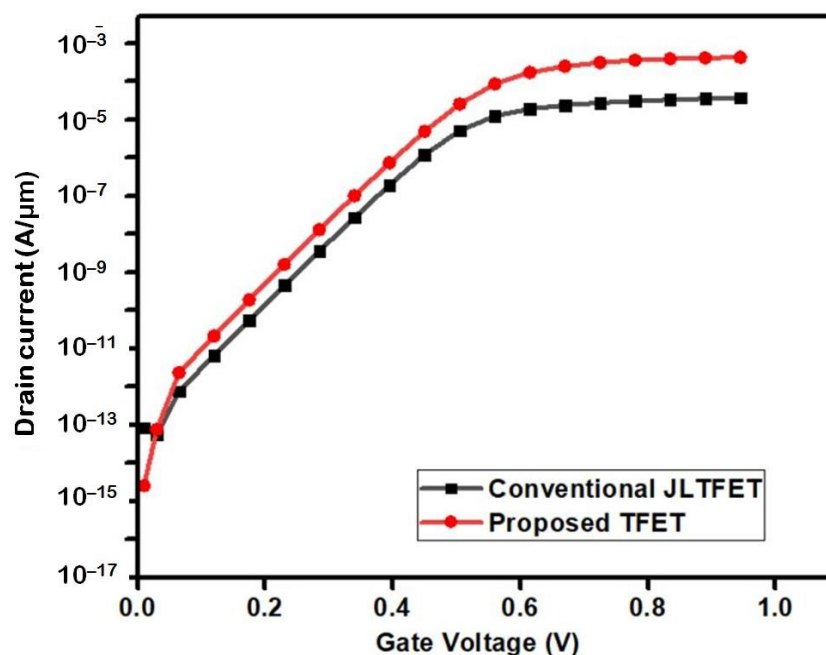


Figure 2. Calibration of the simulated model with a conventional JLTFET.

A list of various parameters for designing the biosensor is presented in Table 1. It is preferred to etch the cavity at the tunnel junction for better impact and control.

Table 1. Parameter values for biosensor design.

Parameters	Values
$L_1$	5 nm
$L_2$	5–10 nm
$L_3$	5–10 nm
$t_{oxf}$	1 nm
$t_{oxb}$	2 nm
$t_b$	1 nm
$t_{si}$	5 nm
$\Phi_{M1}$ (Al)	4.1 eV
$\Phi_{M2}$ (Co)	4.7 eV
$\Phi_{M3}$ (Sc)	4.0 eV
$t_{cavity}$	5–7 nm
$t_{length}$	10–30 nm
Bioanalyte permittivities	$k = 1$ –12

The simulations were performed using the Synopsis TCAD tool [37], and a non-local band was incorporated into the band-tunneling model [38]. The nonlocal model defines the electric field for each mesh and proves to be more accurate. As the device is highly doped, the band-gap-narrowing model is enabled; the Shockley–Read–Hall (SRH) model is included to study the impact of high impurity and interface trap charges; and the trap-assisted tunneling (TAT) model is also included to incorporate the impact of band-to-band tunneling (BTBT) and interface traps. Thus, at the biosensor’s sensing part, a nano-gap is created in the dielectric layer near the source region. A portion is etched using photolithography to create the gap. Thereafter, the source and the drain are created by depositing gate materials with a suitable work function. This is a purely simulation-based approach.

### 3. Analytical Model of Device as Biosensor

The potential distribution is represented by Poisson’s equation as [31]

$$\frac{\partial^2 \phi(x,y)}{\partial x^2} + \frac{\partial^2 \phi(x,y)}{\partial y^2} = \frac{-qN_{ch}}{\epsilon_{si}} \quad (0 \leq x \leq L; 0 \leq y \leq t_{si}), \tag{1}$$

where  $N_{ch}$  denotes the channel doping,  $\epsilon_{si}$  is silicon dielectric permittivity,  $L$  is the control gate length,  $\phi(x, y)$  denotes the channel potential,  $q$  is the elementary electron charge, and  $t_{si}$  is the thickness of the device.  $A_0$  represents the surface potential and  $A_1(x), A_2(x)$  are coefficients and functions of the position on the surface [16].

$$\phi(x, y) = A_0 + A_1(x)y + A_2(x)y^2. \tag{2}$$

The surface potential of different metals is represented as

$$\phi_j(x, y) = A_{0j} + A_{j1}(x)y + A_{j2}(x)y^2. \tag{3}$$

Here,  $j = 1, 2, 3$  for metals M1, M2, M3, respectively; for  $L_{j-1} \leq x \leq L_j$  and  $0 \leq y \leq t_{si}$ ,  $\phi_j$  represents potential. The channel starts at  $L_0$ , and the length of the cavity is  $L_c = L_2 + L_3$ . The use of three gate materials marks the presence of different flat band voltages and work functions.  $\chi$  denotes the electron affinity,  $E_g$  is a band gap at 300 K, and  $\Phi_B$  is the Fermi potential [30].

$$V_{FB,L1} = \Phi_{M1} - \Phi_{Si}, V_{FB,L2} = \Phi_{M2} - \Phi_{Si}, V_{FB,L3} = \Phi_{M3} - \Phi_{Si}, \tag{4}$$

where  $\Phi_{M1}, \Phi_{M2}, \Phi_{M3}$  represent the work functions of different metals, and  $\Phi_{Si}$  is the silicon work function [19,31].

$$\Phi_{Si} = \chi + \frac{E_g}{2q} + \Phi_B, \tag{5}$$

$$\Phi_B = V_T \ln\left(\frac{N_{ch}}{n_i}\right) \tag{6}$$

where  $V_T = \frac{kT}{q}$  is thermal voltage while  $n_i$  represents the intrinsic concentration of silicon. Considering the continuity of the electric field along the front and back gate, we can write [31]

$$\left. \frac{d\phi_1(x,y)}{dy} \right|_{y=0} = -\frac{C_{oxf1} V_{gs1} - A_{01}(x)}{C_s t_{si}}, \tag{7}$$

$$V_{gs1} = V_{gs} - V_{FB,L1}, C_s = \frac{\epsilon_{Si}}{t_{Si}}$$

$$\left. \frac{d\phi_2(x,y)}{dy} \right|_{y=0} = -\frac{C_{oxf2} V_{gs2} - A_{02}(x)}{C_s t_{si}}, V_{gs2} = V_{gs} - V_{FB,L2},$$

$$\left. \frac{d\phi_3(x,y)}{dy} \right|_{y=0} = -\frac{C_{oxf3} V_{gs3} - A_{03}(x)}{C_s t_{si}}, V_{gs3} = V_{gs} - V_{FB,L3}.$$

The capacitance below metal M1 ( $C_{oxf1}$ ) is the combination of the capacitance across the basic dielectric layer ( $C_{oxbasef1}$ ) and the fixed oxide capacitance ( $C_{ofixed}$ ) [29]

$$C_{oxf1} = \frac{C_{oxbase1f} \cdot C_{ofixed}}{C_{oxbase1f} + C_{ofixed}},$$

Layer 3,  $C_{ofixed} = \frac{\epsilon_{SiO_2}}{t_{cavity}}$

$$C_{oxbasef1} = \frac{C_{oxH} \cdot C_{oxs}}{C_{oxH} + C_{oxs}},$$

where

$$\text{Layer 1, } C_{oxH} = \frac{\epsilon_{HfO_2}}{t_{oxf}},$$

$$\text{Layer 2, } C_{oxs} = \frac{\epsilon_{SiO_2}}{t_{oxf}},$$

$C_{oxbasef1}$  = capacitance of basic dielectric layer.  $C_{fixed}$  = capacitance of SiO<sub>2</sub> layer near the cavity.

Again, for metal gate M2, the capacitance of the basic dielectric layer ( $C_{oxbasef2}$ ) is represented as

$$C_{oxbasef2} = \frac{C_{ox2} \cdot C_{ox22}}{C_{ox2} + C_{ox22}},$$

$$\text{Layer 1, } C_{ox2} = \frac{\epsilon_{HfO_2} + \epsilon_{SiO_2}}{t_{oxf}},$$

where

$$\epsilon_{ox2} = \epsilon_{HfO_2} + \epsilon_{SiO_2},$$

$$\text{Layer 2, } C_{ox22} = \frac{\epsilon_{HfO_2}}{t_{oxf}}.$$

Similarly, the basic dielectric layer capacitance across M3 ( $C_{oxbasef3}$ ) is

$$C_{oxbasef3} = \frac{\epsilon_{HfO_2}}{2t_{oxf}},$$

where  $t_{oxf}$  is the thickness of the front oxide, while  $\epsilon_{HfO_2}$  and  $\epsilon_{SiO_2}$  are the dielectric permittivities of HfO<sub>2</sub> and SiO<sub>2</sub>.

As shown in Figure 1, the cavity is formed under metal gates M2 and M3. The biomolecules are trapped under layers M2 and M3, and this changes the capacitance below M2 and M3.

For a fully filled nano gap [16,20],

$$C_{oxfi} = \frac{C_{oxbasefi} \cdot C_{oxbiomolef}}{C_{oxbasefi} + C_{oxbiomolef}}, \quad i = 2, 3 \text{ for M2, M3.} \tag{8}$$

For the cavity where biomolecules are trapped,  $C_{oxbiomolef} = \frac{\epsilon_{biomolecule}}{t_{cavity}}$ .

For a partially filled nano-gap under M2 and M3,

$$C_{oxfi} = \frac{\epsilon_{oxbasei} \cdot \epsilon_{biomolecule} \cdot \epsilon_{air}}{\epsilon_{oxbasei} \cdot t_{air} \cdot t_{cavity} + \epsilon_{biomolecule} \cdot t_{air} \cdot t_{oxf} + \epsilon_{air} \cdot t_{oxf} \cdot t_{cavity}},$$

where  $\epsilon_{oxbase2} = \frac{\epsilon_{ox2} \epsilon_{HfO_2}}{\epsilon_{ox2} + \epsilon_{HfO_2}}$  and  $\epsilon_{oxbase3} = \epsilon_{HfO_2}$ .

Considering the continuity of the electric field at the back gate,  $y = t_{si}$  [31],

$$\left. \frac{d\phi_1(x, y)}{dy} \right|_{y=t_{si}} = - \frac{C_{oxb1} \phi_{B1}(x) - V_{gs1}}{C_s t_{si}}$$

$$\left. \frac{d\phi_2(x, y)}{dy} \right|_{y=t_{si}} = - \frac{C_{oxb2} \phi_{B2}(x) - V_{gs2}}{C_s t_{si}}$$

$$\left. \frac{d\phi_3(x, y)}{dy} \right|_{y=t_{si}} = - \frac{C_{oxb3} \phi_{B3}(x) - V_{gs3}}{C_s t_{si}}$$

Similarly, the basic dielectric layer is fixed, hence,

$$C_{oxb} = \frac{\epsilon_{HfO_2}}{t_{oxb}},$$

$\phi_B$  is the back-gate potential. Thus, for a fully filled nano-gap in the back gate,

$$C_{oxb\ j} = \frac{C_{oxb} \cdot C_{oxb-molecules\ j}}{C_{oxb} + C_{oxb-molecules\ j}}, j = 1, 2, 3,$$

$$C_{oxb-molecules\ j} = \frac{\epsilon_{SiO_2}}{t_{cavity}}.$$

For  $j = 1$ , M1 is

$$C_{oxb-molecules\ j} = \frac{\epsilon_{biomolecule}}{t_{cavity}}, \text{ for } j = 2, 3 \text{ i. e., M2, M3}$$

For a partially filled nano gap under M2 and M3 in the back gate [16]

$$C_{oxfj} = \frac{\epsilon_{HfO_2} \cdot \epsilon_{biomolecule} \cdot \epsilon_{air}}{\epsilon_{HfO_2} \cdot t_{air} \cdot t_{cavity} + \epsilon_{biomolecule} \cdot t_{air} \cdot t_{oxb} + \epsilon_{air} \cdot t_{oxb} \cdot t_{cavity}},$$

$$\phi_B(x, y) = \phi(x, y)|_{y=t_{si}}.$$

$\phi_{Bj}(x, y)$  is the back gate potential for different metals ( $j = 1, 2, 3$ ).  $\phi_{Bj}(x, y) = A_{0j}(x) + A_{j1}(x)t_{si} + A_{j2}(x)t_{si}^2$  for M1, M2, and M3 [30].  $\phi_j(x, y = 0) = A_{0j}$  is the surface potential.

Considering the continuity of the surface potential at the interface [31],

$$\phi_1(L_1, 0) = \phi_2(L_1, 0), \tag{9}$$

$$\phi_2(L_2, 0) = \phi_3(L_2, 0).$$

The electric field continuity at the interface in the lateral direction is

$$\left. \frac{d\phi_1(x, y)}{dy} \right|_{x=L_1} = \left. \frac{d\phi_2(x, y)}{dy} \right|_{x=L_1}, \tag{10}$$

$$\left. \frac{d\phi_2(x, y)}{dy} \right|_{x=L_2} = \left. \frac{d\phi_3(x, y)}{dy} \right|_{x=L_2}.$$

$$\phi_1(0, 0) = V_{bipot} = V_T \ln \left( \frac{N_a N_{ch}}{n_i^2} \right),$$

where  $V_{bipot}$  represents the built-in potential, and  $V_{DS}$  represents the voltage across the drain with respect to the source.

$$N_a = N_d = N_{ch}, \tag{11}$$

as the device is homogeneously doped [26]

$$\phi_3(L_3, 0) = V_{bipot} + V_{DS} = V_T \ln \left( \frac{N_d N_{ch}}{n_i^2} \right). \tag{12}$$

The constants can be evaluated by solving Equation (3). The obtained values are written as

$$A_{11}(x) = - \frac{C_{oxf\ 1} V_{gs1} - A_{01}(x)}{C_s t_{si}}$$

$$A_{21}(x) = - \frac{C_{oxf\ 2} V_{gs2} - A_{02}(x)}{C_s t_{si}}$$

$$A_{31}(x) = - \frac{C_{oxf\ 3} V_{gs3} - A_{03}(x)}{C_s t_{si}}$$

$$A_{12}(x) = \frac{\frac{C_{oxb j}}{C_s t_{si}} \left(1 + \frac{C_{oxf 1}}{C_s} + \frac{C_{oxf 1}}{C_{oxb j}}\right)}{t_{si} \left(2 + \frac{C_{oxf j}}{C_s}\right)} [V_{gs1} - A_{01}(x)]$$

$$A_{22}(x) = \frac{\frac{C_{oxb j}}{C_s t_{si}} \left(1 + \frac{C_{oxf 2}}{C_s} + \frac{C_{oxf 2}}{C_{oxb j}}\right)}{t_{si} \left(2 + \frac{C_{oxf 2}}{C_s}\right)} [V_{gs2} - A_{02}(x)]$$

$$A_{12}(x) = \frac{\frac{C_{oxb j}}{C_s t_{si}} \left(1 + \frac{C_{oxf 3}}{C_s} + \frac{C_{oxf 3}}{C_{oxb j}}\right)}{t_{si} \left(2 + \frac{C_{oxf 3}}{C_s}\right)} [V_{gs3} - A_{03}(x)]$$

Substituting the above values into Equation (3) and comparing the result with Equation (1), we obtain

$$\frac{\partial^2 \phi_j(x)}{\partial x^2} - m_j \phi_j(x) = n_j, \tag{13}$$

where

$$m_j = \frac{2C_{oxb j}}{C_s t_{si}} \left(1 + \frac{C_{oxf j}}{C_s} + \frac{C_{oxf j}}{C_{oxb j}}\right), \tag{14}$$

$$n_j = \frac{-qN_{ch}}{\epsilon_{si}} - \frac{2C_{oxb j}}{C_s t_{si}} V_{gsj} \left(1 + \frac{C_{oxf j}}{C_s} + \frac{C_{oxf j}}{C_{oxb j}}\right).$$

The surface potentials under the three regions are provided below:

$$\phi_1(x) = U \exp(\lambda_1 x) + V \exp(-\lambda_1 x) - \frac{n_1}{m_1}, \tag{15}$$

$$\phi_2(x) = W \exp(\lambda_2(x - L_1)) + X \exp(-\lambda_2(x - L_1)) - \frac{n_2}{m_2}, \tag{16}$$

$$\phi_3(x) = Y \exp(\lambda_3(x - L_1 - L_2)) + \exp(-\lambda_3(x - L_1 - L_2)) - \frac{n_3}{m_3},$$

where

$$\lambda_j = \sqrt{m_j}, j = 1, 2, 3$$

To determine the boundary condition constants, Equation (6) is used:

$$U = V_{bipot} - V + \frac{n_1}{m_1}$$

$$W = U \exp(\lambda_1 L_1) + \frac{n_2}{m_2} - \frac{n_1}{m_1}$$

$$X = V \exp(-\lambda_1 L_1) + \frac{n_2}{m_2} - \frac{n_1}{m_1}$$

$$Y = \exp(-\lambda_3 L_3) + \left[ (V_{bipot} + V_{DS}) + \frac{n_3}{\alpha_3} - Z \exp(-\lambda_3 L_3) \right]$$

$$P_1 = -\frac{n_1}{m_1}, P_2 = -\frac{n_2}{m_2}, P_3 = -\frac{n_3}{m_3}, D = \frac{C_1}{C_2},$$

$$C_1 = \exp(-\lambda_1 L_1 + 2\lambda_3 L_3) + \exp(\lambda_1 L_1)$$

$$C_2 = \exp(-\lambda_1 L_1 + 2\lambda_3 L_3) - \exp(\lambda_1 L_1)$$



$$E = 2D \cosh(\lambda_2 L_2) - 2 \sinh(\lambda_2 L_2)$$

$$V = \frac{(V_{bipot} + V_{DS}) + \exp(-(\lambda_1 L_1 + \lambda_3 L_3)(1-D))}{E} + \frac{D(P_3 - P_2)}{E} + \frac{P_3 \exp(-(\lambda_1 L_1 + \lambda_3 L_3)(D-1) + V_{bipot} + \exp(\lambda_2 L_2)(1-D) + P_1 \exp(\lambda_2 L_2)(1-D))}{E} + \frac{(D(P_1 - P_2) \cosh(\lambda_2 L_2 - \lambda_1 L_1) - \sinh(\lambda_2 L_2 - \lambda_1 L_1))}{E}$$

$$Z = \frac{2V \sinh(\lambda_2 L_2)}{C_2} + \frac{P_1 \exp(\lambda_2 L_2)}{C_2} + \frac{(P_2 - P_3)}{C_2} + \frac{(V_{bipot} + V_{DS}) + \exp(-(\lambda_1 L_1 + \lambda_3 L_3))}{C_2} + \frac{V_{bipot} \exp(\lambda_2 L_2) - [(P_1 - P_2) \cosh(\lambda_2 L_2 - \lambda_1 L_1)] - [P_3 \exp(-(\lambda_1 L_1 + \lambda_3 L_3))]}{C_2}$$

The expression for the lateral electric field is derived as

$$E_{1x}(x) = - \left. \frac{d\phi_1(x,y)}{dx} \right|_{y=0} = -U \lambda_1 \exp(\lambda_1 x) + V \lambda_1 \exp(\lambda_1 x),$$

$$E_{2x}(x) = - \left. \frac{d\phi_2(x,y)}{dx} \right|_{y=0} = -W \lambda_2 \exp(\lambda_2(x - L_1)) + X \lambda_2 \exp(-\lambda_2(x - L_1)),$$

$$E_{3x}(x) = - \left. \frac{d\phi_3(x,y)}{dx} \right|_{y=0} = Y \lambda_3 \exp(\lambda_3(x - L_1 - L_2)) + Z \lambda_3 \exp(-\lambda_3(x - L_1 - L_2)).$$

The vertical electric field is

$$E_{1y}(x) = - \frac{d\phi_1(x,y)}{dy} = -A_{11}(x) - 2yA_{12}(x),$$

$$E_{2y}(x) = - \frac{d\phi_2(x,y)}{dy} = -A_{21}(x) - 2yA_{22}(x)$$

$$E_{3y}(x) = - \frac{d\phi_3(x,y)}{dy} = -A_{31}(x) - 2yA_{32}(x)$$

The expression for the current is obtained using Kane’s model [2,24] as

$$I_D = q \int G_{BTB} dv \tag{17}$$

$$G_{BTB} = A_{kane} \frac{|E|^2}{\sqrt{E_g}} \exp \left[ -B_{kane} \frac{E_g^{\frac{3}{2}}}{|E|} \right]$$

$E$  is the average electric field, and  $E_g$  is the energy bandgap.

$$A_{kane} = 4 \times 10^{14} \text{ V}^{-\frac{5}{2}} \text{ s}^{-1} \text{ cm}^{-\frac{1}{2}}; B_{kane} = 1.9 \times 10^7 \frac{\text{V}}{\text{cm}}$$

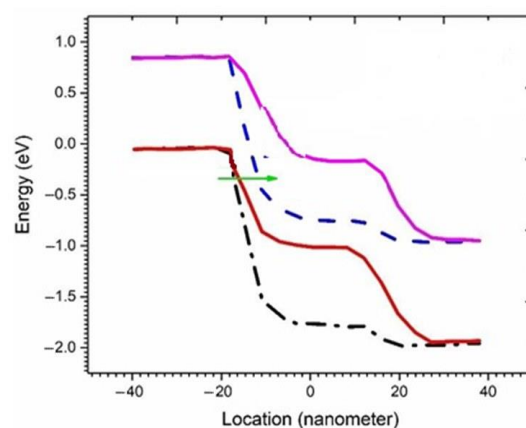
Thus, the modeling of the TFET design can be initiated with the basic Poisson equation; then, the standard solution is represented by Equation (2). Depending on the device architecture, the materials used can be modified and represented in the equations. Finally, the surface potential and electric fields are computed and a continuity relation is applied. Once we obtain the electric field, we can also compute the drain current using Kane’s relation.

In a TFET-based biosensor, the main architecture change occurs only in the cavity region, which impacts the capacitance calculation. Thus, the capacitance in each region needs to be calculated.

#### 4. Results and Discussions

The energy band of the proposed biosensor is shown in Figure 3. As the dielectric permittivity across the cavity increases, the electric field maximizes, and, therefore, the best possible alignment occurs. The dotted line shows the alignment when a dielectric

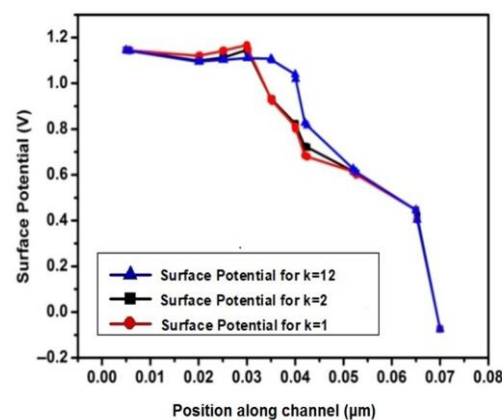
with a permittivity of  $k = 12$  fills the cavity, whereas the straight line shows the situation for  $k = 1$  (air). It was observed that there is less alignment between the bands for a cavity filled with air. If the energy bands that are aligned are higher, the tunneling width decreases, and thus, the probability of carrier tunneling is better. The green arrow in the figure depicts the tunnel width.



**Figure 3.** Energy band diagram of a DM-JLTFET as a biosensor for  $k = 12$  (dashed and dash-dotted lines) and  $k = 1$  (solid lines). The green arrow shows the tunnel width.

#### 4.1. Validation of the Proposed Structure and Its Mathematical Model

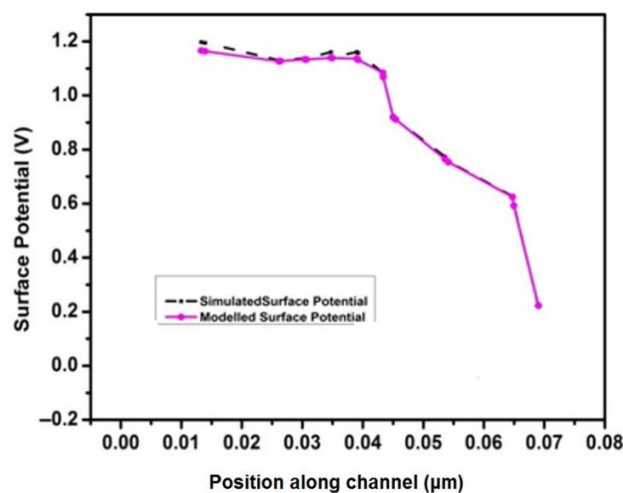
The performance of the proposed structure is validated by comparing it with the existing structures, as shown in Table 2. Similarly, the surface potential model is depicted in Figure 4 for various dielectrics. The variation in the potential along the channel is studied. It was observed that the potential drops across the channel. The step change in the potential profile is due to the use of three different materials across the control gate. The potential profile then drops to zero in the source region. Because of the higher effective capacitance caused by the increased dielectric permittivity,  $k$ , the barrier width at the source-channel junction drops, resulting in a rapid rise in the surface potential across the tunneling area. Thereafter, the modeled and simulated values of the surface potential are compared in Figure 5. The graph demonstrates the congruence of the surface potential values between those that were modeled and those that were simulated, thus proving the viability of the suggested model.



**Figure 4.** Surface potential along the channel for different permittivities.

**Table 2.** A comparison with reference works.

References	$I_{ON}$ (A/ $\mu\text{m}$ )	$I_{OFF}$ (A/ $\mu\text{m}$ )	Ratio	$V_{th}$ (V)	SS (Average) mV/dec	SS (Point) mV/dec
Ref. [25]	$36 \times 10^{-6}$	$5 \times 10^{-14}$	$6 \times 10^8$	0.4	70	38
Ref. [30]	$1 \times 10^{-6}$	$1 \times 10^{-13}$	$6 \times 10^7$	0.8	48	-
Ref. [39]	$18 \times 10^{-5}$	$3 \times 10^{-13}$	$6 \times 10^8$	0.4	-	17
Present work ( $k = 12$ )	$3 \times 10^{-4}$	$2.4 \times 10^{-17}$	$1.2 \times 10^{13}$	0.3	48	9

**Figure 5.** Comparison of surface potential values along the microchannel—analytical model (solid lines) vs. simulation (dashed).

#### 4.2. Drain Current Variation for Different Values of $k$ for Electrically Neutral Biomolecules

The current variation for different dielectrics in fully filled nano-gaps is shown in Figure 6. The analyte materials selected are air ( $k = 1.0$ ), biotin ( $k = 2.0$ ), ferro-cytochrome ( $k = 4$ ), bacteriophage T7 ( $k = 6$ ), zein ( $k = 7$ ), keratin ( $k = 9$ ), and gelatin ( $k = 12$ ), as shown in Table 3. The similarity between the analytically modeled and simulated values shows the accuracy of the proposed model. The gate oxide across the tunnel junction is etched to create biosensor cavities. Following that, analyte molecules with different dielectric permittivities, such as keratin, gelatin, etc., are filled into these cavities. Capacitances vary because of changes in the analyte dielectric permittivity. The ensuing change in capacitance causes a shift in the charge density across the junction, boosting the surface potential and, in turn, increasing the electric field across the junction. Thus, higher electric fields result in better coupling and thereby increase the current density, which is responsible for higher tunneling as the permittivity rises, and this results in a high current.

**Table 3.** Dielectric permittivity values.

Parameters	Values for $k$
Air	1
Ferro-cytochrome	4
Biotin	2
Bacteriophage T7	6
Zein	7
Keratin	9
Gelatin	12

The selectivity of our sensor can be boosted in the usual way by functionalizing its sensing surface by attaching receptors to it that specifically bind the targeted analyte (ligand), thus vastly improving the affinity. Some of the convenient receptor–ligand pairs applied to a TFET with a source cavity are quoted in a paper by Soni et al. [40]. For the current sensor architecture, the specific binding occurs mainly via the cavity approach, wherein the dielectric modulation-based label-free sensing technique is used, thus ensuring the proper transduction of the amount of the targeted analyte to a proportional modification of the output electric signals. Consequently, a significant increase can be seen in the device surface potentials. This will result in a considerable increase in the charge carriers, which will intensify the abruptness across the junction. The capacitance will be impacted by this shift as well, which will alter the electric field, and thus, the drain current will also change.

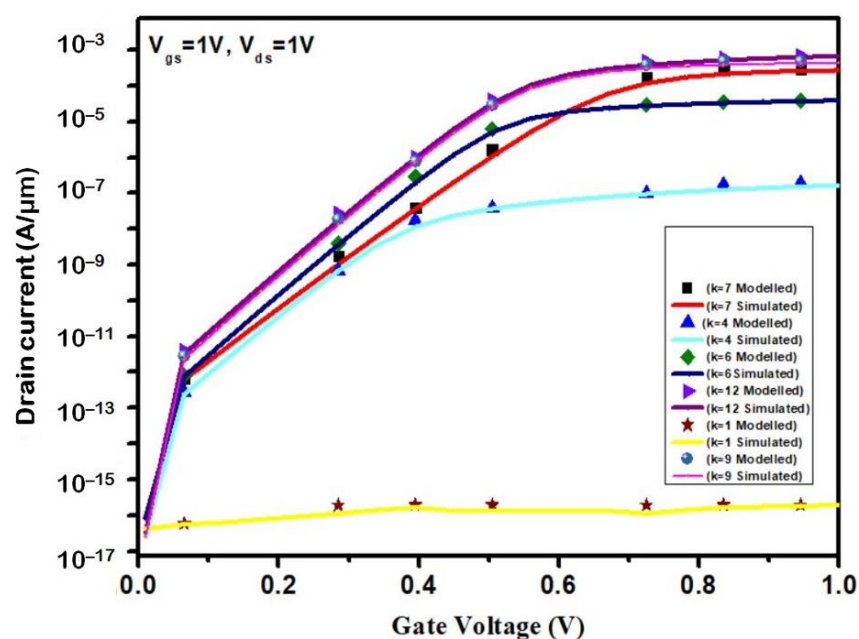


**Figure 6.** Variation in drain current versus gate voltage for biomolecules with different values of dielectric permittivity: a comparison of analytical and simulated results.

This technique can also be used for measurements of a typical sample of dilute biomolecules in a solution. For biological applications, it is critical to correctly identify biomarkers in clinically pertinent samples. By injecting a solution into the cavity surface that does not contain the desired biomolecule (blank), a baseline for the device’s current can be established for a typical sample. When the solution containing the biomolecule is subsequently added, the device’s current changes right away and finally stabilizes. Ref. [27] described a similar method of dilute biomolecule detection.

#### 4.3. Effect of Variation of Drain Current with Length of Cavity

The cavity length varies from 10 nm to 30 nm, keeping  $k = 12$  and the cavity thickness at 5 nm, while the gate voltage is maintained at 1 V and the drain voltage at 1 V. The drain current gate voltage dependence for different cavity lengths is shown in Figure 7. It was observed that, for a length of 10 nm, the current sensitivity is quite low, and if the length increases to 20 nm, the ON current raises. However, if we further increase the length, there is a small decrease in the drain current. Moreover, the OFF current remains almost constant. This behavior is due to the fact that, for a 20 nm cavity, the maximum electric field appears at the tunnel junction, and the energy bands are perfectly aligned. Thus, the maximum number of carriers can tunnel across the junction, resulting in an increase in the

drain current. As we further increase the length, the alignment is impaired, and the tunneling reduces. The modeling and simulation results show similar values (overlapping in the figure).

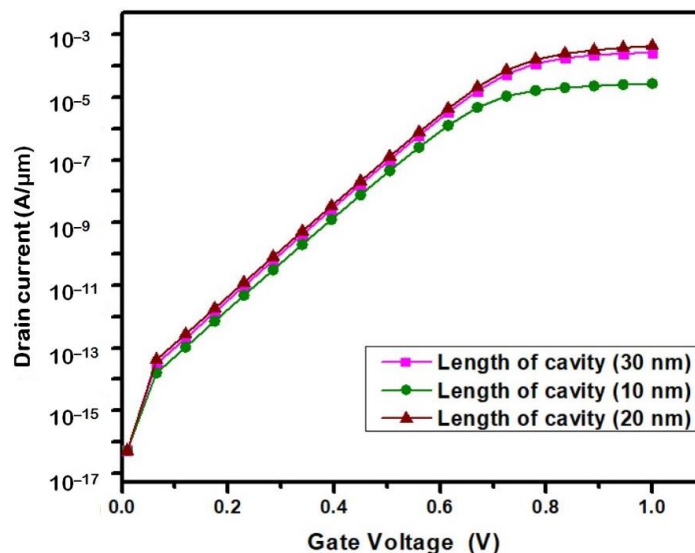


Figure 7. Drain current versus gate voltage for different cavity lengths.

#### 4.4. Effect of Drain Current Variation with Cavity Thickness

The impact of drain current variation on the thickness of the cavity is shown in Figure 8. The length of the cavity, the gate voltage, and the drain voltage are kept fixed at 20 nm, 1 V, and 1 V, respectively. It was found that, as the thickness increases, the effective tunneling barrier widens, and it becomes difficult for the carriers to tunnel across the junction. Therefore, as the carrier tunneling reduces, the drain current consequently decreases. Because of poor gate control in the channel area, the current drops as the thickness rises while the threshold voltage rises.

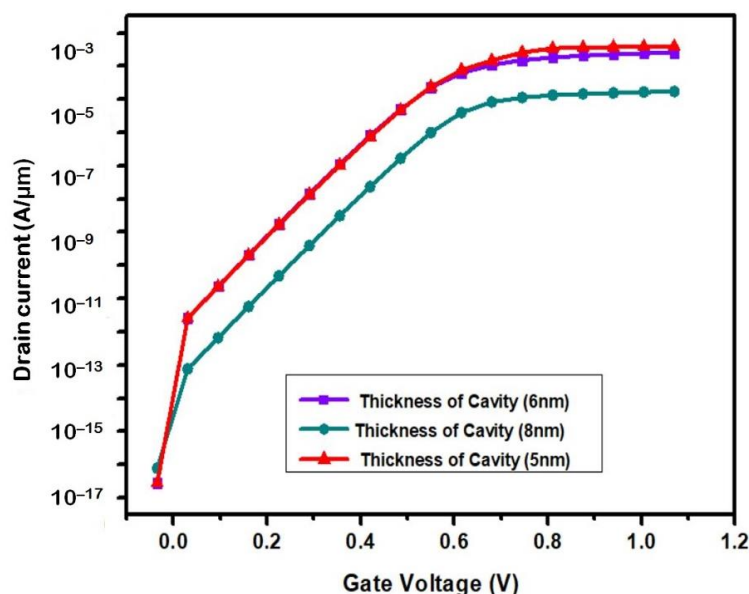


Figure 8. Drain current versus gate voltage for different values of the cavity thickness.

#### 4.5. Effects of Electrically Charged Biomolecules

The impact of electrically charged (positive/negative) biomolecules in a fully filled nano-gap is depicted in Figure 9. The graph shows that the drain current rises with an increase in positive charges (a left shift of the characteristics), whereas it decreases with an increase in negative charges (a right shift). This can be represented by the MOSFET equation [32]:

$$V_{GS} = \psi_s + \phi_{ms} - \frac{qN_{bio}}{C_{ox'}}, \quad C_{ox'} = \frac{k}{t_{ox}}, \quad (18)$$

where the symbols have their usual meaning.

The charge in a biomolecule significantly depends on pH. In our simplified model, proteins and nucleic acids, as charged macromolecules, are represented by the charges of their ionizable residues. The measurement of charges is carried out at a particular pH. Some experimental ranges for charges in biomolecules, as mentioned in [41], at pH 7 are shown here (a charge of 1.0 e for Arg and Lys; a charge of 1.0 e for Glu and Asp). As mentioned in [42], biotin has a pI of 3.5, where pI signifies the isoelectric point. The isoelectric point is the pH value where a molecule exhibits a neutral net charge. For any value below pI, the biomolecule exhibits a positive surface charge, and above that, it represents a negative surface charge. Similarly, streptavidin has a pI value of 5.5.

Conventionally, most of the reported TFET-based biosensors were tested for a charge range of  $-5 \times 10^{11}$  to  $+5 \times 10^{12}$ .

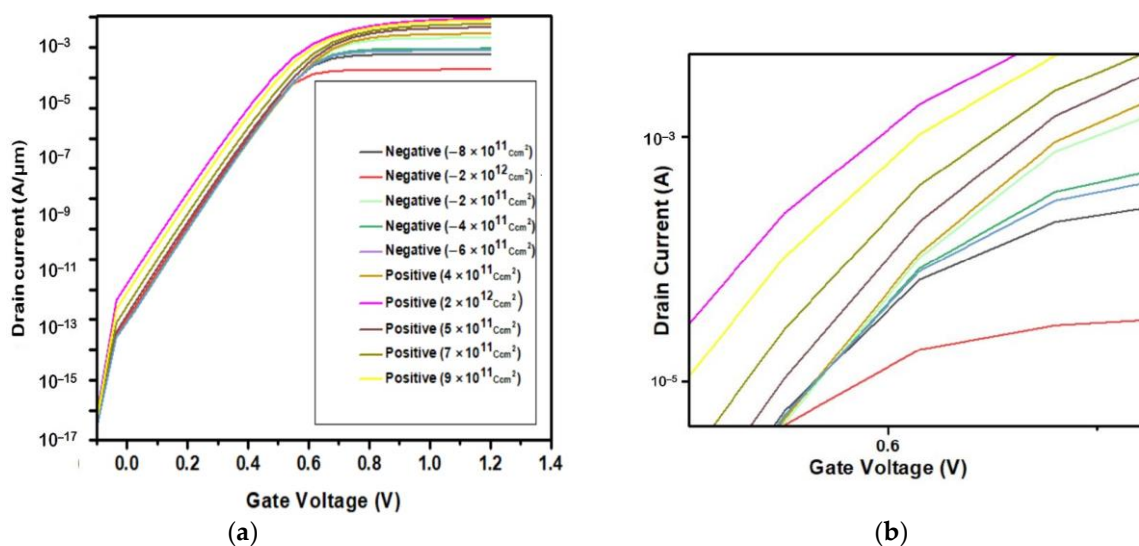


**Figure 9.** (a) Drain current versus gate voltage for different values of electric charge in biomolecules. (b) Enlarged part of the current–voltage dependence shown in (a).

##### 4.5.1. Threshold Voltage and Sensitivity Analysis for Negatively Charged Biomolecules

The impact of a negative charge of  $-1 \times 10^{12}$  C/cm<sup>2</sup> with variation in dielectric permittivity is plotted in Figure 10a. As depicted in Figure 10b, the sensitivity shows a declining trend as the negative charge increases. However, for a fixed charge, the sensitivity increases with  $k$ . As shown in Figure 10c, the drain current shifts toward the right with an increase in negative charge, and thus, the threshold voltage increases. However, for a fixed charge, the threshold voltage increases with  $k$ . According to Equation (18), for a fixed gate voltage, the surface potential declines with an increase in negative charges, and thus, the current also declines.

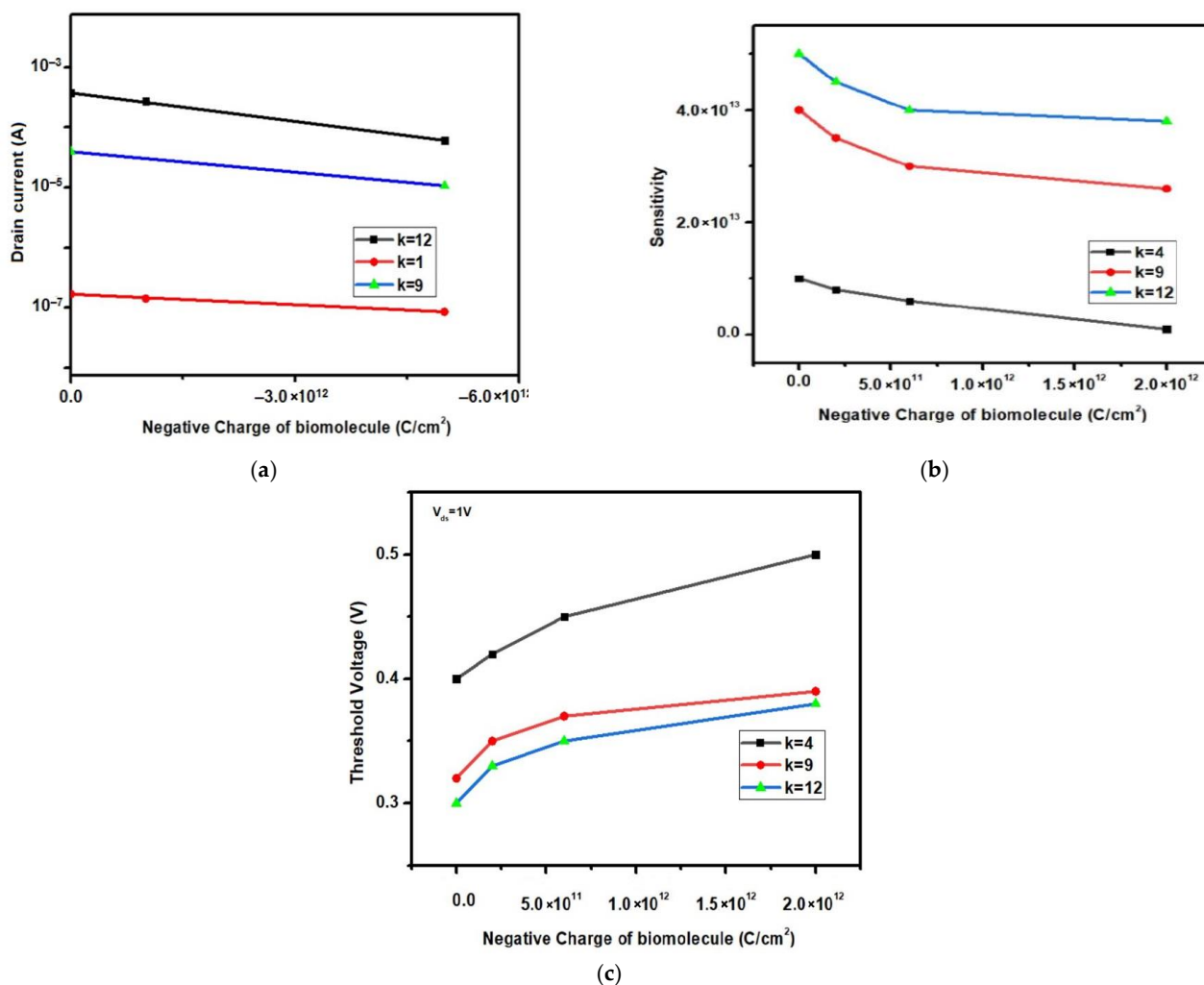


**Figure 10.** (a) Drain current for negative molecules,  $-1 \times 10^{12} C/cm^2$  with permittivity variation. (b) Sensitivity as a function of a negative charge with permittivity variation. (c) Threshold voltage as a function of negative charge with permittivity variation.

#### 4.5.2. Threshold Voltage and Sensitivity Analysis for Positively Charged Biomolecules

The impact of a positive charge of  $1 \times 10^{12} C/cm^2$  with variation in dielectric permittivity is plotted in Figure 11a. As depicted in Figure 11b, the sensitivity increases as the magnitude of the positive charge increases. However, for a fixed charge, the sensitivity increases with the  $k$  value. As shown in Figure 11c, the drain current shifts toward the left with an increase in the positive charge, resulting in a decrease in the threshold voltage. However, for a fixed charge, the threshold voltage increases with the  $k$  value.

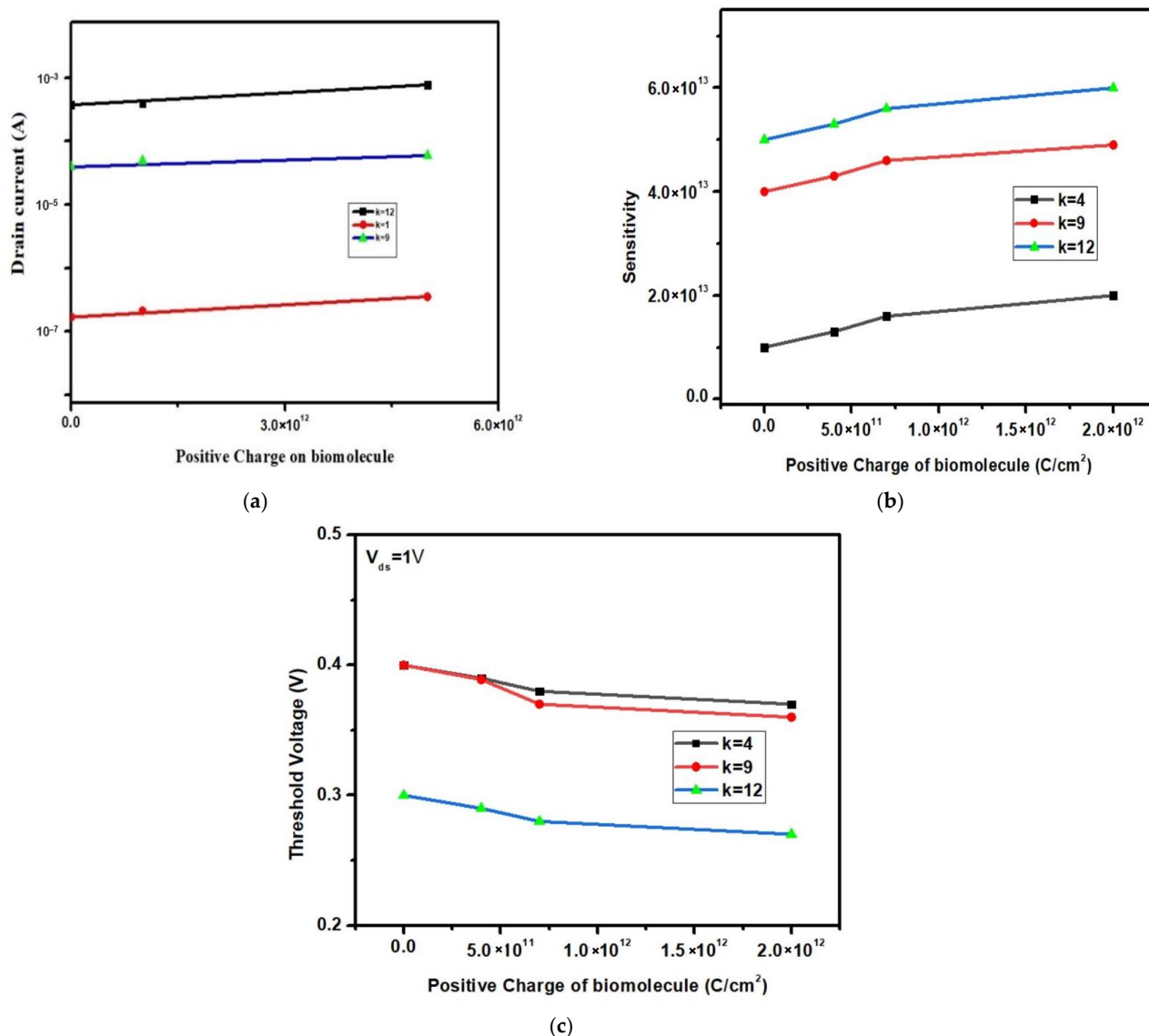


**Figure 11.** (a) Drain current for positive molecules,  $1 \times 10^{12}$  C/cm<sup>2</sup> with permittivity variation. (b) Sensitivity as a function of a positive charge. (c) Threshold voltage as a function of a positive charge.

#### 4.6. Impact of Fill Factor

The performance of a biosensor depends on the fraction of the cavity filled with biomolecules. Figure 12 shows the impact of the fill factor on the drain current when the cavities are 100% filled, 75% filled, and 25% filled. When the cavity is fully filled, the drain current increases, as the gate can exert maximum control over the channel, and the current increases. As the fill factor declines, the cavity has a lower number of biomolecules, and the rest of the cavity is filled with air. This means that the capacitance reduces, and this in turn results in a drop in the electric field across the tunnel junction. Thus, the current declines with a reduction in the fill factor.



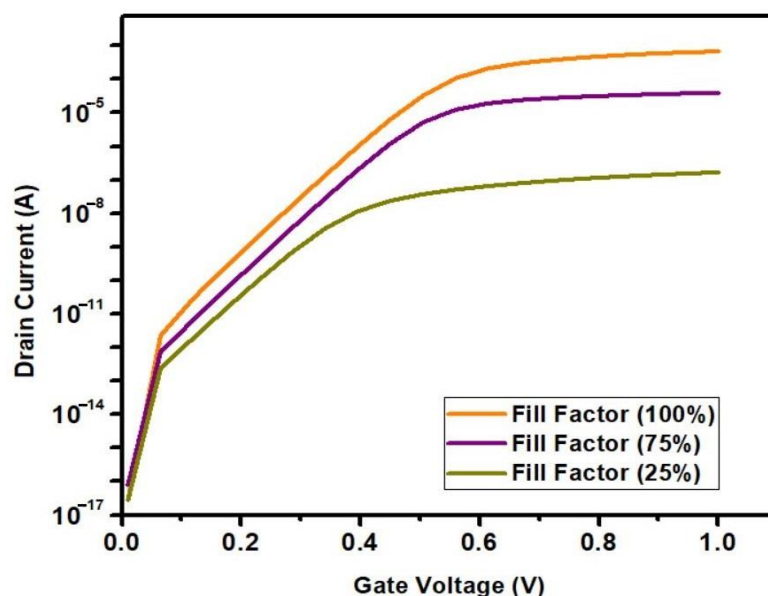
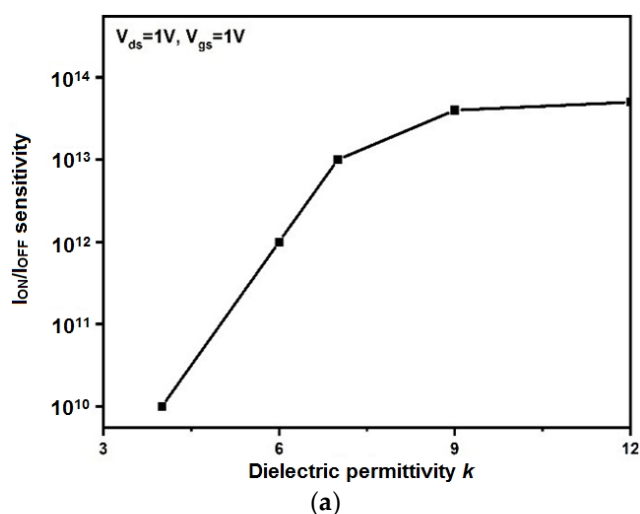
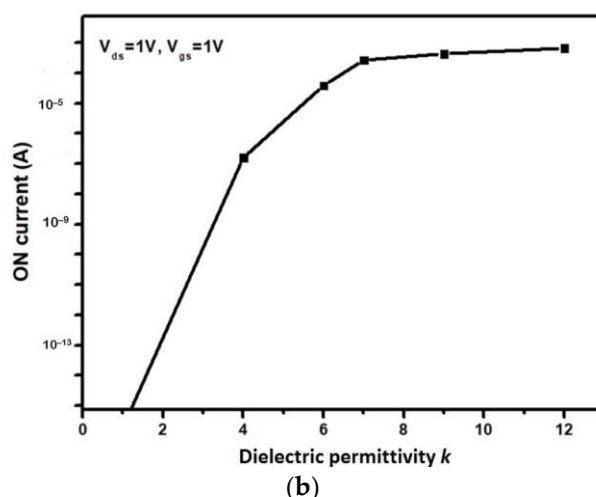


Figure 12. Drain current versus gate voltage for various fill factors.

#### 4.7. Sensitivity Analysis

A shift in current with a change in the dielectric value is known as current sensitivity. The dielectric permittivity across the polar gate is kept fixed, whereas cavities are etched in the control gate across the tunnel junction. The performance is assessed by filling the cavities with biomolecules of different dielectrics. The performance is studied for both analyte-filled ( $k = 12$ ) and empty cavities ( $k = 1$ ), i.e., air-filled. The current sensitivity is determined as the ratio of the current when the cavity is filled with biomolecules of  $k = 12$  to the current when the cavity is filled with air for a fixed gate voltage, as shown in Figure 13. As the dielectric permittivity increases, the capacitance across the cavity also increases. As a result of the resulting change in capacitance, the charge density across the junction shifts, raising the surface potential, and, consequently, the electric field across the junction increases. A higher electric field results in better coupling, leading to improved tunneling efficiency and resulting in a higher ON current. The OFF current remains more or less unaffected, thereby improving the overall current ratio.





**Figure 13.** (a) Current sensitivity (ON/OFF current ratio) dependence on  $k$ -value. (b) ON current dependence on  $k$ -value.

#### 4.7.1. Current Sensitivity

The current sensitivity calculation can be presented as follows:

$$S_{current} = \frac{I_D^{Bio}}{I_D^{Air}} \Big|_{V_{gs}} = \frac{10^{-4}}{10^{-17}} = 10^{13}$$

The current sensitivity in the presence of biomolecules with a permittivity,  $k$ , is  $I_D^{Bio} = 10^{-4}$ . The current sensitivity in an empty cavity with  $k = 1$  (air) is  $I_D^{Air} = 10^{-17}$ .  $V_{gs} = \text{constant}$ .

#### 4.7.2. Threshold Voltage Sensitivity

The threshold voltage ( $V_{th}$ ) sensitivity calculation can be presented as follows:

$$S_{voltage} = V_{th}(\text{air}, k = 1) - V_{th}(\text{bioanalyte}, k = 12) = 1 \text{ V} - 0.3 \text{ V} = 0.7 \text{ V}$$

#### 4.8. Impact of Dielectric Permittivity Variation on Current Ratio (Current Sensitivity)

The impact of the variation in the dielectric constant of the material on the drain current and current ratio is depicted in Figure 13. The ON current increases with the  $k$ -value as the alignment of the band improves with an increasing dielectric permittivity. This is due to the fact that as the dielectric value increases, the gate control across the tunnel junction also improves. Moreover, with an increase in the dielectric permittivity value, the capacitance across the tunnel junction increases; i.e., the charge carrier concentration across the junction rises, which, in turn, increases the electric field across the junction. Thus, a better alignment is achieved. Moreover, as the OFF current remains almost the same, the current ratio also increases, and hence, the relative sensitivity also improves.

#### 4.9. Impact of Dielectric Permittivity Variation on Threshold Voltage

The effect of dielectric permittivity variation on threshold voltage is shown in Figure 14. The threshold voltage is calculated by the constant current method at a  $10^{-7}$  value for the ON current. We found that the threshold voltage thereby declines with a rise in the  $k$  value. As the  $k$  value increases; the coupling improves; the band alignment becomes better because of the increased electric field; and, hence, the tunneling probability becomes higher.

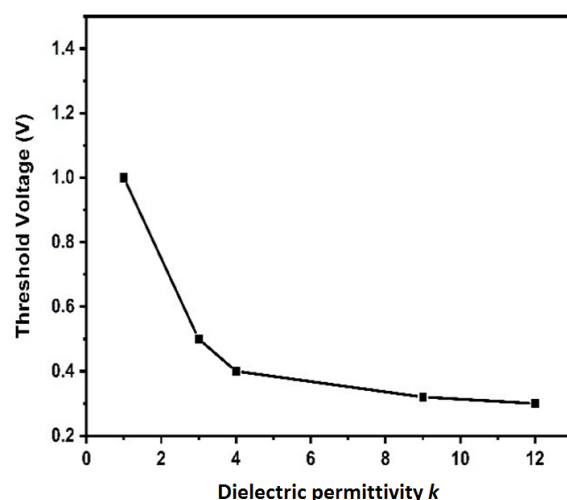


Figure 14. Threshold voltage dependence on dielectric permittivity.

#### 4.10. Impact of Dielectric Permittivity on Subthreshold Swing (SS)

One of the important parameters that determines the switching speed is the SS [43].

$$SS = \frac{\partial V_{gs}}{\partial \log I_{ds}} \text{ mV/dec.}$$

The SS of a TFET depends significantly on the tunneling phenomenon [38]. The plot in Figure 15 reflects that, for neutral biomolecules, SS decreases with an increase in the  $k$ -value. This is due to the fact that, as mentioned in the previous subsection, a higher  $k$  value will result in a higher electric field, which is why the tunneling probability increases.

$$\Delta SS = \frac{SS_{air} - SS_{bio}}{SS_{air}} = \frac{72 - 48}{72} = 0.33 \text{ mV/dec}$$

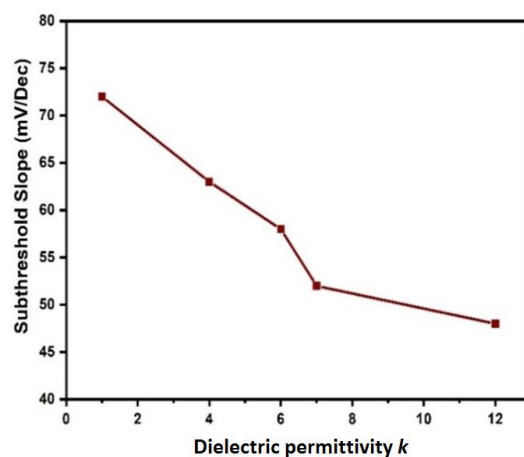


Figure 15. Subthreshold slope dependence on dielectric permittivity,  $d$ .

#### 4.11. Comparison with Literature

A comparative survey presented in Table 4 shows that the proposed JLTFET can achieve current sensitivities two orders of magnitude higher than competing TFET-based devices from the literature. In other words, this device is capable of achieving  $I_{ON}/I_{OFF}$  sensitivity in the range of  $10^{13}$  for current and 0.7 V for voltage change.

Table 4. Comparison of different TFET-based biosensor designs.

References	$I_{ON}/I_{OFF}$	$\Delta V_{th}$ , V	$\Delta SS$ , mV/dec
Ref. [26]	$10^{10}$	0.45	0.25

Ref. [32]	10 <sup>11</sup>	-	-
Ref. [34]	10 <sup>10</sup>	0.7	-
Ref. [35]	10 <sup>9</sup>	0.7	-
Present work	10 <sup>13</sup>	0.7	0.33

## 5. Conclusions

This work discusses the application of JLTFT-based biosensors for the detection of various biomolecules. Both the relative current sensitivity and the voltage sensitivity of the proposed sensor are analyzed, and values of 10<sup>13</sup> and 0.7 V are reported. The analytical model of the proposed device is developed. It is solved and validated using the Sentaurus TCAD software. The impact of the position, the electric charge of the biomolecules, the fill factor, and the size of the cavity are also studied. The device not only exhibits a significantly improved relative current sensitivity in comparison with the existing FET and TFET-based biosensors but also shows itself to be practical for low-power uses. Thus, a dielectric-modulation-based design opens a pathway to improved performance and offers a wide range of possibilities for future research and applications.

**Author Contributions:** Conceptualization, S.C.; methodology, S.C. and K.L.B.; software, S.C.; validation, K.L.B., K.G., J.I. and Z.J.; formal analysis, S.C.; investigation, S.C.; design and simulation, S.C.; writing—original draft preparation, S.C.; writing—review and editing, S.C., K.L.B., K.G., J.I., Z.J. and O.J.; visualization, S.C.; supervision, K.L.B.; project administration, K.L.B. and K.G.; funding acquisition, K.G., J.I., Z.J. and O.J. All authors have read and agreed to the published version of the manuscript.

**Funding:** All authors besides O.J. declare that no funds, grants, or other support were received during the preparation of this manuscript. O.J. declares that her work was supported by the Ministry of Science, Technological Development, and Innovations of the Republic of Serbia through grant 451-03-47/2023-01/200026.

**Institutional Review Board Statement:** Not applicable.

**Informed Consent Statement:** Not applicable.

**Data Availability Statement:** Data and materials supporting the research are found within the manuscript. Raw data files will be provided by the corresponding author upon request.

**Acknowledgments:** This publication is an outcome of the R&D work undertaken for the project under the Visvesvaraya Scheme of the Ministry of Electronics and Information Technology, Government of India, implemented by the Digital India Corporation (formerly Media Lab Asia).

**Conflicts of Interest:** The authors declare no conflicts of interest.

## References

- Cui, Y.; Wei, Q.; Park, H.; Lieber, C.M. Nanowire nano-sensors for highly sensitive and selective detection of biological and chemical species. *Science* **2001**, *293*, 1289–1292. <https://doi.org/10.1126/science.1062711>.
- Yang, N.; Chen, X.; Ren, T.; Zhang, P.; Yang, D. Carbon nanotube-based biosensors. *Sens. Actuators B Chem.* **2015**, *207*, 690–715. <https://doi.org/10.1016/j.snb.2014.10.040>.
- Byon, H.R.; Choi, H.C. Network single-walled carbon nanotube-field effect transistors (SWNT-FETs) with increased Schottky contact area for highly sensitive biosensor applications. *J. Am. Chem. Soc.* **2006**, *128*, 2188–2189. <https://doi.org/10.1021/ja056897n>.
- Tang, X.; Bansaruntip, S.; Nakayama, N.; Yenilmez, E.; Chang, Y.I.; Wang, Q. Carbon nanotube DNA sensor and sensing mechanism. *Nano Lett.* **2006**, *6*, 1632–1636. <https://doi.org/10.1021/nl060613v>.
- Star, J.C.; Gabriel, P.; Bradley, K.; Grüner, G. Electronic detection of specific protein binding using nanotube FET devices. *Nano Lett.* **2003**, *3*, 459–463. <https://doi.org/10.1021/nl0340172>.
- Alam, M.Z.; Alimuddin; Khan, S.A. A Review on Schiff Base as a Versatile Fluorescent Chemo-sensors Tool for Detection of Cu<sup>2+</sup> and Fe<sup>3+</sup> Metal Ion. *J. Fluoresc.* **2023**, *13*, 1–32. <https://doi.org/10.1007/s10895-022-03102-1>.
- Alam, M.Z.; Khan, S.A. A review on Rhodamine-based Schiff base derivatives: Synthesis and fluorescent chemo-sensors behaviour for detection of Fe<sup>3+</sup> and Cu<sup>2+</sup> ions. *J. Coord. Chem.* **2023**, *76*, 371–402. <https://doi.org/10.1080/00958972.2023.2183852>.
- Naresh, V.; Lee, N. A Review on Biosensors and Recent Development of Nanostructured Materials-Enabled Biosensors. *Sensors* **2021**, *21*, 1109. <https://doi.org/10.3390/s21041109>.

9. Singh, A.; Sharma, A.; Ahmed, A.; Sundramoorthy, A.K.; Furukawa, H.; Arya, S.; Khosla, A. Recent Advances in Electrochemical Biosensors: Applications, Challenges, and Future Scope. *Biosensors* **2021**, *11*, 336. <https://doi.org/10.3390/bios11090336>.
10. Chen, C.; Wang, J. Optical biosensors: An exhaustive and comprehensive review. *Analyst* **2020**, *145*, 1605–1628. <https://doi.org/10.1039/c9an01998g>.
11. Karimi-Maleh, H.; Orooji, Y.; Karimi, F. A critical review on the use of potentiometric based biosensors for biomarkers detection. *Biosens. Bioelectron.* **2021**, *184*, 113252. <https://doi.org/10.1016/j.bios.2021.113252>.
12. Ramanathan, K.; Danielsson, B. Principles and applications of thermal biosensors. *Biosens. Bioelectron.* **2001**, *16*, 417–423. [https://doi.org/10.1016/s0956-5663\(01\)00124-5](https://doi.org/10.1016/s0956-5663(01)00124-5).
13. Narang, R.; Saxena, M.; Gupta, M. Comparative Analysis of Dielectric-Modulated FET and TFET-Based Biosensor. *IEEE Trans. Nanotechnol.* **2015**, *14*, 427–435. <https://doi.org/10.1109/TNANO.2015.2396899>.
14. Kataoka, H.; Miyahara, Y. Label-free detection of DNA by field-effect devices. *IEEE Sens. J.* **2011**, *11*, 3153–3160. <https://doi.org/10.1109/JSEN.2011.2167143>.
15. Sarkar, S.; Banerjee, K. Fundamental limitations of conventional-FET biosensors: Quantum-mechanical-tunneling to the rescue. In Proceedings of the 70th Device Research Conference, University Park, PA, USA, 18–20 June 2012; pp. 83–84. <https://doi.org/10.1109/DRC.2012.6256950>.
16. Narang, R.; Reddy, K.V.S.; Saxena, M.; Gupta, R.S.; Gupta, M. A Dielectric-Modulated Tunnel-FET-Based Biosensor for Label-Free Detection: Analytical Modeling Study and Sensitivity Analysis. *IEEE Trans. Electron Devices* **2012**, *59*, 2809–2817. <https://doi.org/10.1109/TED.2012.2208115>.
17. Narang, R.; Saxena, M.; Gupta, R.S.; Gupta, M. Dielectric Modulated Tunnel Field-Effect Transistor—A Biomolecule Sensor. *IEEE Electron Device Lett.* **2012**, *33*, 266–268. <https://doi.org/10.1109/LED.2011.2174024>.
18. Kanungo, S.; Chattopadhyay, S.; Gupta, P.S.; Rahman, H. Comparative Performance Analysis of the Dielectrically Modulated Full-Gate and Short-Gate Tunnel FET-Based Biosensors. *IEEE Trans. Electron Devices* **2015**, *62*, 994–1001. <https://doi.org/10.1109/TED.2015.2390774>.
19. Anam, A.; Anand, S. and Amin, S.I. Design and Performance Analysis of Tunnel Field Effect Transistor With Buried Strained Si1-xGex Source Structure Based Biosensor for Sensitivity Enhancement. *IEEE Sens. J.* **2020**, *20*, 13178–13185. <https://doi.org/10.1109/JSEN.2020.3004050>.
20. Narang, R.; Saxena, M.; Gupta, R.S.; Gupta, M. Analytical Model for a Dielectric Modulated Double Gate FET (DM-DG-FET) Biosensor. In Proceedings of the International Conference on Emerging Electronics, Bangalore, India, 11–14 December 2022, pp. 1–4. <https://doi.org/10.1109/ICEmElec.2012.6636256>.
21. Shafi, N.; Sahu, C.; Periasamy, C. Virtually doped Si-Ge tunnel FET for enhanced sensitivity in biosensing applications. *Superlattices Microstruct.* **2018**, *120*, 75–89. <https://doi.org/10.1016/j.spmi.2018.05.006>.
22. Anand, S.; Singh, A.; Amin, S.I.; Thool, A.S. Design and performance analysis of dielectrically modulated doping-less tunnel FET-based label free biosensor. *IEEE Sens. J.* **2019**, *19*, 4369–4374. <https://doi.org/10.1109/JSEN.2019.2900092>.
23. Narang, R.; Saxena, M.; Gupta, M. Modeling and simulation investigation of sensitivity of symmetric split gate Junctionless FET for biosensing application. *IEEE Sens. J.* **2017**, *17*, 4853–4861. <https://doi.org/10.1109/JSEN.2017.2716102>.
24. Singh, S.; Raj, B.; Vishvakarma, S.K. Analytical modeling of split gate junction-less transistor for a biosensor application. *Sens. Biosens. Res.* **2018**, *18*, 31–36. <https://doi.org/10.1016/j.sbsr.2018.02.001>.
25. Ghosh, B.; Akram, M.W. Junction less Tunnel Field Effect Transistor. *IEEE Electron Device Lett.* **2013**, *34*, 584–586. <https://doi.org/10.1109/LED.2013.2253752>.
26. Chakraborty, A.; Singha, D.; Sarkar, A. Staggered heterojunctions-based tunnel-FET for application as a label-free biosensor. *Int. J. Nanopart.* **2018**, *10*, 107–116. <https://doi.org/10.1504/IJNP.2018.092681>.
27. Gao, N.; Lu, N.; Wang, Y. Robust ultrasensitive tunneling-FET biosensor for point-of-care diagnostics. *Sci. Rep.* **2016**, *6*, 22554. <https://doi.org/10.1038/srep22554>.
28. Choudhury, S.; Baishnab, K.L.; Bhowmik, B.; Guha, K. Design and optimization of asymmetrical TFET. In *Microsystem Technologies*; Springer, SCI: Berlin/Heidelberg, Germany, 2021; Volume 27, pp. 3457–3464. <https://doi.org/10.1007/s00542-020-05140-w>.
29. Gupta, S.K.; Kumar, S. Analytical Modeling of a Triple Material Double Gate TFET with Hetero-Dielectric Gate Stack. *Silicon* **2018**, *11*, 1355–1369. <https://doi.org/10.1007/s12633-018-9932-y>.
30. Darwin, S.; ASTS. Mathematical Modeling of Junctionless Triple Material Double Gate MOSFET for Low Power Applications. *J. Nano Res.* **2019**, *56*, 71–79. <https://doi.org/10.4028/www.scientific.net/jnanor.56.71>.
31. Priya, G.L.; Balamurugan, N.B. New dual material double gate junctionless tunnel FET: Subthreshold modeling and simulation. *AEU Int. J. Electron. Commun.* **2019**, *99*, 130–138. <https://doi.org/10.1016/j.aeue.2018.11.037>.
32. Im, H.; Huang, X.J.; Gu, B.; Choi, Y.K. A dielectric-modulated field-effect transistor for biosensing. *Nat. Nanotechnol.* **2007**, *2*, 430–434. <https://doi.org/10.1038/nnano.2007.180>.
33. Sharma, D.; Singh, D.; Pandey, S.; Yadav, S.; Kondekar, P.N. Comparative analysis of full-gate and short-gate dielectric modulated electrically doped Tunnel-FET based biosensors. *Superlattice Microstruct.* **2017**, *111*, 767–775. <https://doi.org/10.1016/j.spmi.2017.07.035>.
34. Venkatesh, P.; Nigam, K.; Pandey, S.; Yadav, S.; Kondekar, P.N. A dielectrically modulated electrically doped tunnel FET for application of label free biosensor. *Superlattice Microstruct.* **2017**, *109*, 470–479. <https://doi.org/10.1016/j.spmi.2017.05.035>.
35. Verma, M.; Tirkey, S.; Yadav, S.; Sharma, D.; Yadav, D.S. Performance assessment of a novel vertical dielectrically modulated TFET-based biosensor. *IEEE Trans. Electron Devices* **2017**, *64*, 3841–3848. <https://doi.org/10.1109/TED.2017.2732820>.

36. Devi, W.V.; Bhowmick, B. Optimization of Pocket doped Junctionless TFET and its Application in digital Inverter. *Micro Nano Lett.* **2018**, *14*, 69–73. <https://doi.org/10.1049/mnl.2018.5086>.
37. INTERNATIONAL. *International Technology Roadmap for Semiconductor*; INTERNATIONAL: New York, NY, USA, 2018. Available online: [Ieee.org](http://www.ieee.org) (accessed on 28 July 2022).
38. Hussain, S. A comprehensive study on tunneling field effect transistor using non-local band-to-band tunneling model. *J. Phys. Conf. Ser.* **2020**, *1432*, 012028. <https://doi.org/10.1088/1742-6596/1432/1/012028>.
39. Bal, P.; Ghosh, B.; Mondal, P. Dual material gate junctionless tunnel field effect transistor. *J. Comput. Electron.* **2014**, *13*, 230–234. <https://doi.org/10.1007/s10825-013-0505-4>.
40. Soni, D.; Sharma, D.; Aslam, M.; Yadav, S. Approach for the improvement of sensitivity and sensing speed of TFET-based biosensor by using plasma formation concept. *Micro Nano Lett.* **2018**, *13*, 1728–1733. <https://doi.org/10.1049/mnl.2018.5252>.
41. Zweckstetter, M.; Hummer, G.; Bax, A. Prediction of Charge-Induced Molecular Alignment of Biomolecules Dissolved in Dilute Liquid-Crystalline Phases. *Biophys. J.* **2004**, *86*, 3444–3460. ISSN 0006-3495. <https://doi.org/10.1529/biophysj.103.035790>.
42. Lee, J.; Kim, M.J.; Yang, H.; Kim, S.; Yeom, S.; Ryu, G.; Shin, Y.; Sul, O.; Jeong, J.K.; Lee, S.-B. Extended-Gate Amorphous InGaZnO Thin Film Transistor for Biochemical Sensing. *IEEE Sens. J.* **2020**, *21*, 178–184. <https://doi.org/10.1109/JSEN.2020.3014447>.
43. Kanungo, S.; Chattopadhyay, S.; Gupta, P.S. Study and analysis of the effects of Si-Ge source and pocket doped channel on sensing performance of dielectrically modulated tunnel FET based biosensor. *IEEE Trans. Electron Devices* **2016**, *63*, 2589–2596. <https://doi.org/10.1109/TED.2016.2556081>.

**Disclaimer/Publisher’s Note:** The statements, opinions and data contained in all publications are solely those of the individual author(s) and contributor(s) and not of MDPI and/or the editor(s). MDPI and/or the editor(s) disclaim responsibility for any injury to people or property resulting from any ideas, methods, instructions or products referred to in the content.